



interest in this technique is supported by its numerous potential applications namely non-destructive testing, homeland security and the study of composite materials used in aircraft industry [2, 3]. Recent works in medical imaging suggest possible advantages in diagnosis since images exhibit better contrast in certain scenarios such as lung tumors [4, 5]. The first formulation of Compton tomography based on a Radon type transform has been introduced by Norton in [1]. The mathematical foundations arising from the seminal works of Allan Cormack on circular Radon transforms provide a formal framework to study these modalities [6, 7, 8]. In two dimensional scanning, a collimated source is used to restrict photons to a plane. Depending on the setup, forward models are based on integral transforms on different manifolds. When collimated detectors are used, manifolds are circular arcs [1, 9, 10, 11, 12, 13] or pairs of circular arcs [2]. When collimator is removed from detectors, manifolds are toric sections [3, 14]. In three dimensional Compton scatter tomography uncollimated source and detectors are employed. The problem has recently been addressed in rotational [15] as well as translational geometries [16] where results on uniqueness, injectivity and numerical reconstruction have been reported. Four three dimensional modalities were introduced in [17] together with a filtered-backprojection algorithm for contour reconstruction. Issues on stability have also been raised and microlocal analysis used to address them in particular families of toric sections [18] and toric surfaces [19].

Here, we introduce a novel Compton scatter tomography in three dimensions with fixed source and unique detector. This setup is an extension of a recently developed Compton scatter tomography modality in two dimensions [13] whose design has some material advantages, namely compactness and simplicity, that make it attractive for implementation. The extension to three dimensions by means of the removal of the collimator at the source may provide extra advantages like faster scanning and a higher signal level. In order to model the forward problem, we introduce a Radon transform on tori and study its properties, particularly those connected to its invertibility. The paper is organized as follows. In section 2 we explain briefly the setup, the scanning protocol and the toric Radon transform used to model image formation. In section 3, we use spherical harmonics to find an Abel's type equation relating the coefficients of the expansion of the data with those of the function that represents the electronic density of an object. In section 4, we show the uniqueness of the solution of this equation and, thus, the invertibility of the toric Radon transform. Numerical reconstructions based on discrete spherical harmonics and Tikhonov regularization are presented in section 5. We analyze our results as well as some new perspectives of our work in section 6 and, finally, we close the paper with some conclusions. The algorithm for discrete spherical harmonic expansion is set aside and discussed in Appendix A.

## **2. A new setup for three dimensional Compton scatter tomography**

We introduce a setup for Compton scatter tomography based on a central source of radiation  $S$  located at the origin of coordinates. A single detector  $D$  moves at a constant

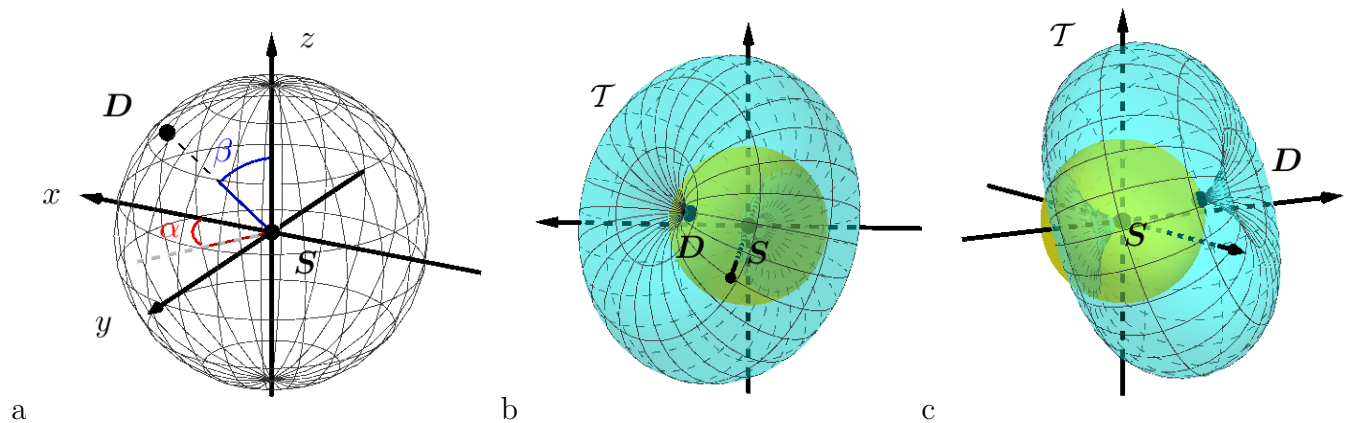


**Figure 1.** a: setup of the new CST modality: source ( $S$ ), detector ( $D$ ), detection sphere (mesh). b and c: two views of an apple torus  $\mathcal{T}$  (blue) and the detection sphere (yellow).

distance  $R$  of the origin describing a sphere, as shown in figure 1. The property to recover is the electronic density  $f(x, y, z)$  of an object placed outside this spherical surface. Detector  $D$  registers backscattered photons of energy  $E(\omega)$  that have interacted with electrons of the object and deviated an angle  $\omega$  from its original path. When detector  $D$  is at position labeled by angles  $(\alpha, \beta)$  and registers a photon of energy  $E(\omega)$ , the interaction site is located somewhere on the surface of an apple torus through points  $S$  and  $D$ , which is characterized by  $\alpha$ ,  $\beta$  and  $\omega$ . Thus, the flux of photons of energy  $E(\omega)$  registered by  $D$  at sites  $(\alpha, \beta)$  is proportional to the integral of function  $f$  on a toric surface  $\mathcal{T}^{\omega, \alpha, \beta}$ , with  $\alpha \in [0, 2\pi)$ ,  $\beta \in [0, \pi]$  and  $\omega \in (\pi/2, \pi)$ , see figures 1 and 2. Notice that the referred torus may be generated by the rotation of a toric section around segment  $\overline{SD}$ , see figure 2.

Before giving the definition of the Radon transform modeling the direct problem, let us introduce some notation. The coordinates of the detector  $D$  are given by

$$D(\alpha, \beta) = R \begin{pmatrix} \cos \alpha \sin \beta \\ \sin \alpha \sin \beta \\ \cos \beta \end{pmatrix}, \quad \alpha \in [0, 2\pi), \beta \in [0, \pi].$$

We define a parametrization of any torus  $\mathcal{T}^{\omega, \alpha, \beta}$  as:

$$\Phi^{\omega, \alpha, \beta}(\gamma, \psi) = r^\omega(\gamma) \Theta^{\alpha, \beta}(\gamma, \psi), \quad (1)$$

with  $\gamma \in (0, \omega)$ ,  $\psi \in (0, 2\pi)$ . Here, the radial part is given by

$$r^\omega(\gamma) = R \frac{\sin(\omega - \gamma)}{\sin \omega}$$

while the angular part is expressed as  $\Theta^{\alpha, \beta}(\gamma, \psi) = u(\alpha) a(\beta) \Theta(\gamma, \psi)$ , where

$$\Theta(\gamma, \psi) = \begin{pmatrix} \cos \psi \sin \gamma \\ \sin \psi \sin \gamma \\ \cos \gamma \end{pmatrix}$$

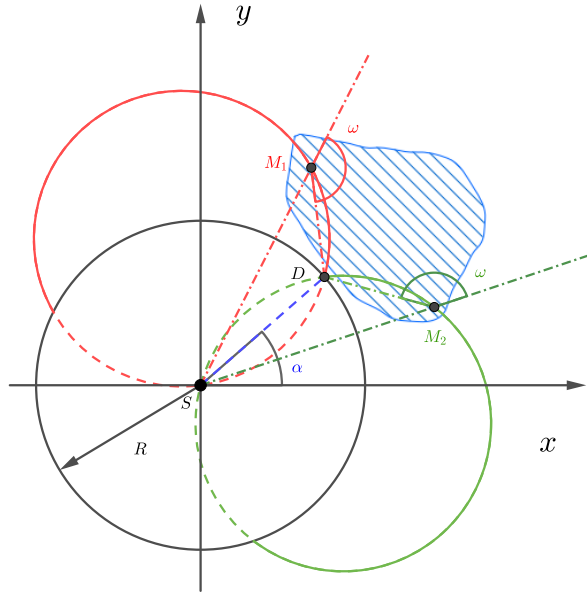


**Figure 2.** Planar section ( $z = 0$ ) of the setup and the manifold. Toric section (continuous curves red and green) rotates around  $\overline{SD}$  to generate the torus.  $S$ : source,  $D$ : detector,  $\omega$ : scattering angle,  $M_1$  and  $M_2$ : scattering sites,  $R$ : radius of the detection sphere. In this case, the detector is placed at angles  $\alpha < \pi/2$  and  $\beta = \pi/2$

is a point on  $S^2$ , the unit sphere in  $\mathbb{R}^3$ , and

$$u(\alpha) = \begin{pmatrix} \cos \alpha & -\sin \alpha & 0 \\ \sin \alpha & \cos \alpha & 0 \\ 0 & 0 & 1 \end{pmatrix} \quad \text{and} \quad a(\beta) = \begin{pmatrix} \cos \beta & 0 & \sin \beta \\ 0 & 1 & 0 \\ -\sin \beta & 0 & \cos \beta \end{pmatrix} \quad (2)$$

are a rotation of angle  $\alpha$  about the  $z$  axis and a rotation of angle  $\beta$  about the  $y$  axis, respectively. Finally, given positive numbers  $r_M, r_m$  such that  $r_M > r_m > R > 0$ , we define the hollow sphere  $S_h(r_m, r_M)$  as

$$S_h(r_m, r_M) = \{(x, y, z) \in \mathbb{R}^3 : r_m \leq \sqrt{x^2 + y^2 + z^2} \leq r_M\}.$$

We are now ready to introduce the toric Radon transform.

**Definition.** Let  $f(x, y, z)$  be a compact supported function with support contained in  $S_h(r_m, r_M)$ . We define the toric Radon transform  $\mathcal{R}_{\mathcal{T}}f$  of function  $f$  as  $\mathcal{R}_{\mathcal{T}}f(\alpha, \beta, \omega) = \int_{\mathcal{T}} dS_{\mathcal{T}} f(x, y, z)$ . Explicitly

$$\mathcal{R}_{\mathcal{T}}f(\alpha, \beta, \omega) = \int_0^\omega d\gamma \int_0^{2\pi} d\psi f(\Phi^{\omega, \alpha, \beta}(\gamma, \psi)) r^\omega(\gamma) \frac{\sin \gamma}{\sin \omega}, \quad (3)$$

where  $\omega \in (\frac{\pi}{2}, \pi)$ ,  $\alpha \in [0, 2\pi)$ ,  $\beta \in [0, \pi]$ .

Equation (3) is the forward formula that models the data recorded.

### 3. Relation between data and object in the Fourier domain

In this section, we find a connection between the components of the spherical harmonics expansion (or Fourier expansion) of a function  $f$  and those of its toric Radon transform  $\mathcal{R}_{\mathcal{T}}f(\alpha, \beta, \omega)$ . We show that they are connected through a generalized Abel integral equation.

#### 3.1. Basics of spherical harmonics

We introduce some definitions and properties of spherical harmonics that are relevant in what follows. For a full treatment of the topic see [20, 21, 22].

*3.1.1. Definition* Spherical harmonics of degree  $l$  and order  $m$  are defined as:

$$Y_l^m(\gamma, \psi) = (-1)^m \sqrt{\frac{(2l+1)(l-m)!}{4\pi(l+m)!}} P_l^m(\cos \gamma) e^{im\psi}, \quad (4)$$

where  $\gamma \in [0, \pi]$ ,  $\psi \in [0, 2\pi)$  and  $P_l^m(x)$  is the Legendre polynomial of degree  $l$  and order  $m$ . The set  $\{Y_l^m\}$ , for  $l \in \mathbb{N}$  and  $|m| \leq l$  is a complete orthonormal system in  $S^2$ . So, any function  $f \in C^\infty(\mathbb{R}^3)$  can be expanded in terms of  $Y_l^m(\gamma, \psi)$  according to

$$f(r\Theta(\gamma, \psi)) = \sum_{l=0}^{\infty} \sum_{|m| \leq l} f_{lm}(r) Y_l^m(\gamma, \psi), \quad (5)$$

where

$$f_{lm}(r) = \langle f, Y_l^m \rangle = \int_0^{2\pi} \int_0^\pi f(r\Theta(\gamma, \psi)) \overline{Y_l^m(\gamma, \psi)} \sin \gamma \, d\gamma d\psi,$$

$\langle, \rangle$  is the scalar product in  $L^2(S^2)$ , the overline denotes complex conjugation, and  $r \in \mathbb{R}$  is fixed.

*3.1.2. Rotation properties* Given  $h^{-1} = u(\alpha)a(\beta)$  we define the rotation operator  $\Lambda_h$  by its action on a function  $f$  as:

$$(\Lambda_h f)(r\Theta(\gamma, \psi)) = f(rh^{-1}\Theta(\gamma, \psi)). \quad (6)$$

Applying this linear operator  $\Lambda_h$  in (5) we have

$$(\Lambda_h f)(r\Theta(\gamma, \psi)) = \sum_{l \in \mathbb{N}} \sum_{|m| \leq l} f_{lm}(r) (\Lambda_h Y_l^m)(\gamma, \psi). \quad (7)$$

Properties (i)-(iii) will be useful in what follows:

- (i) Any rotated spherical harmonic of degree  $l$  is a linear combination of  $Y_l^n$  with  $|n| \leq l$ :

$$(\Lambda_h Y_l^m)(\gamma, \psi) = \sum_{|n| \leq l} Y_l^n(\gamma, \psi) D_{n,m}^{(l)}(h), \quad (8)$$

(ii) Matrices  $D^{(l)}(h)$  verify:

$$D_{0,m}^{(l)}(h) = \overline{D_{m,0}^{(l)}(h^{-1})}. \quad (9)$$

(iii) From the definition of the matrix entries  $D_{n,m}^{(l)}(h)$  [20], it follows that:

$$Y_l^m(\alpha, \beta) = \sqrt{\frac{2l+1}{4\pi}} \overline{D_{m,0}^{(l)}(h^{-1})}. \quad (10)$$

See [20] and [21] for details.

### 3.2. Spherical harmonic expansion of $\mathcal{R}_{\mathcal{T}}f$

In this section we work out the spherical harmonic expansion of  $\mathcal{R}_{\mathcal{T}}f$ , following the ideas in [15]. First, let us express the spherical harmonic expansion of  $\mathcal{R}_{\mathcal{T}}f$  as

$$\mathcal{R}_{\mathcal{T}}f(\alpha, \beta, \omega) = \sum_{l \in \mathbb{N}} \sum_{|m| \leq l} (\mathcal{R}_{\mathcal{T}}f)_{lm}(\omega) Y_l^m(\alpha, \beta). \quad (11)$$

Observe that the coefficients  $(\mathcal{R}_{\mathcal{T}}f)_{lm}(\omega)$  depend on the scattering angle  $\omega$ .

**Theorem 3.1.** *The Fourier coefficients of data  $(\mathcal{R}_{\mathcal{T}}f)_{lm}$  and those of the object  $f_{lm}$  are related by*

$$(\mathcal{R}_{\mathcal{T}}f)_{lm}(\omega) = 2\pi \int_0^\omega d\gamma r^\omega(\gamma) \frac{\sin \gamma}{\sin \omega} f_{lm}(r^\omega(\gamma)) P_l^0(\cos \gamma), \quad (12)$$

where  $P_l^0(\cdot)$  is the zero order associated Legendre polynomial of degree  $l$ .

*Proof.* From (3) and (6) we have:

$$\mathcal{R}_{\mathcal{T}}f(\alpha, \beta, \omega) = \int_0^\omega d\gamma \int_0^{2\pi} d\psi r^\omega(\gamma) \frac{\sin \gamma}{\sin \omega} (\Lambda_h f)(r^\omega(\gamma) \Theta(\gamma, \psi)). \quad (13)$$

Using (7) and (8), we can write:

$$\begin{aligned} \mathcal{R}_{\mathcal{T}}f(\alpha, \beta, \omega) &= \sum_{l \in \mathbb{N}} \sum_{|m| \leq l} \int_0^\omega d\gamma \int_0^{2\pi} d\psi r^\omega(\gamma) \frac{\sin \gamma}{\sin \omega} f_{lm}(r^\omega(\gamma)) (\Lambda_h Y_l^m)(\gamma, \psi) \\ &= \sum_{l \in \mathbb{N}} \sum_{|m| \leq l} \sum_{|n| \leq l} \int_0^\omega d\gamma \int_0^{2\pi} d\psi r^\omega(\gamma) \frac{\sin \gamma}{\sin \omega} f_{lm}(r^\omega(\gamma)) Y_l^n(\gamma, \psi) D_{n,m}^{(l)}(h). \end{aligned} \quad (14)$$

Now, using (4) and performing the integration on variable  $\psi$ , we have that the only non-vanishing term is the  $n = 0$  term, so:

$$\begin{aligned}
 \mathcal{R}_{\mathcal{T}}f(\alpha, \beta, \omega) &= \sum_{l \in \mathbb{N}} \sum_{|m| \leq l} \sum_{|n| \leq l} \\
 &\int_0^\omega d\gamma \int_0^{2\pi} d\psi r^\omega(\gamma) \frac{\sin \gamma}{\sin \omega} f_{lm}(r^\omega(\gamma)) (-1)^n \sqrt{\frac{(2l+1)(l-n)!}{4\pi(l+n)!}} P_l^n(\cos \gamma) e^{im\psi} D_{n,m}^{(l)}(h) \\
 &= \sum_{l \in \mathbb{N}} \sum_{|m| \leq l} 2\pi \int_0^\omega d\gamma r^\omega(\gamma) \frac{\sin \gamma}{\sin \omega} f_{lm}(r^\omega(\gamma)) P_l^0(\cos \gamma) \sqrt{\frac{(2l+1)}{4\pi}} D_{0,m}^{(l)}(h) \\
 &= \sum_{l \in \mathbb{N}} \sum_{|m| \leq l} \sqrt{\frac{(2l+1)}{4\pi}} D_{0,m}^{(l)}(h) 2\pi \int_0^\omega d\gamma r^\omega(\gamma) \frac{\sin \gamma}{\sin \omega} f_{lm}(r^\omega(\gamma)) P_l^0(\cos \gamma). \tag{15}
 \end{aligned}$$

Then, using properties (9) and (10) we arrive to

$$\mathcal{R}_{\mathcal{T}}f(\alpha, \beta, \omega) = \sum_{l \in \mathbb{N}} \sum_{|m| \leq l} Y_l^m(\alpha, \beta) 2\pi \int_0^\omega d\gamma r^\omega(\gamma) \frac{\sin \gamma}{\sin \omega} f_{lm}(r^\omega(\gamma)) P_l^0(\cos \gamma). \tag{16}$$

Finally, the factor accompanying the  $l, m$ -spherical harmonic is the  $l, m$ -coefficient of the Fourier expansion of  $(\mathcal{R}_{\mathcal{T}}f)$  in terms of the scattering angle  $\omega$  and we get (12). This completes the proof.  $\square$

#### 4. The invertibility of the toric Radon transform and other properties

We want to address the question of the uniqueness of the solutions of (3). To this end, we use the spherical harmonic expansion of function  $\mathcal{R}_{\mathcal{T}}f$  and analyze the properties of equation (12) and its kernel. Relation (12) is a generalized Abel type integral equation. This kind of equations has been extensively studied and there are theorems on their solution for non-vanishing kernels. In general, equation (12) may be written as

$$\forall t \in [a, b] : g(t) = \int_a^t ds f(s) \frac{1}{\sqrt{t-s}} K(t, s) \tag{17}$$

where  $g \in C([a, b])$  and  $K \in C(\Delta(a, b))$ , with  $\Delta(a, b) := \{a \leq s \leq t \leq b\}$ , is a continuous kernel having zeros on the diagonal, i.e.  $t = s$ . Theorem 4.1 states the conditions for the uniqueness of the solution of a generalized Abel equation with kernels with zeros on its diagonal. It was proved by Schiefeneder and Haltmeier in [23].

**Theorem 4.1.** *If  $K : \Delta(a, b) \rightarrow \mathbb{R}$ , where  $a < b$ , satisfies the following assumptions:*

- (i)  $K \in C^3(\Delta(a, b))$
- (ii)  $N_K := \{s \in [a, b] | K(s, s) = 0\}$  is finite and consist of simple roots.
- (iii) For every  $s \in N_K$ , the gradient  $(\beta_1, \beta_2) = \nabla K(s, s)$  satisfies

$$1 + \frac{1}{2} \frac{\beta_1}{\beta_1 + \beta_2} > 0.$$

Then, for any  $g \in C([a, b])$ , equation (17) has at most one solution in  $f \in C([a, b])$ .

In order to show the uniqueness of the solution of (12) we write it in a suitable form to verify the assumptions in Theorem 4.1 according to [23].

First of all, we split up the integral in two parts having integration range  $(0, \omega - \frac{\pi}{2})$  and  $(\omega - \frac{\pi}{2}, \omega)$ , respectively and perform the substitution  $\gamma = \omega - \sin^{-1}\left(\frac{r \sin \omega}{R}\right)$  in the first integral and  $\gamma = \omega + \sin^{-1}\left(\frac{r \sin \omega}{R}\right) - \pi$  in the second one. Taking into account the support of function  $f$  for the lower limit of integration range to  $\left[R, \frac{R}{\sin \omega}\right]$  we may write

$$\begin{aligned} (\mathcal{R}_{\mathcal{T}}f)_{lm}(\omega) &= \frac{2\pi}{\sin \omega} \int_R^{\frac{R}{\sin \omega}} dr r f_{lm}(r) s^-(\omega, r) P_l^-(\omega, r) \frac{1}{\sqrt{\left(\frac{R}{\sin \omega}\right)^2 - r^2}} \\ &\quad + \frac{2\pi}{\sin \omega} \int_{\frac{R}{\sin \omega}}^R dr r f_{lm}(r) s^+(\omega, r) P_l^+(\omega, r) \frac{1}{\sqrt{\left(\frac{R}{\sin \omega}\right)^2 - r^2}} \end{aligned} \quad (18)$$

where

$$\begin{aligned} s^-(\omega, r) &= -\sin\left(\omega - \sin^{-1}\left(\frac{r \sin \omega}{R}\right)\right) \\ P_l^-(\omega, r) &= P_l^0\left(\cos\left(\omega - \sin^{-1}\left(\frac{r \sin \omega}{R}\right)\right)\right) \\ s^+(\omega, r) &= \sin\left(\omega + \sin^{-1}\left(\frac{r \sin \omega}{R}\right) - \pi\right) \\ P_l^+(\omega, r) &= P_l^0\left(\cos\left(\omega + \sin^{-1}\left(\frac{r \sin \omega}{R}\right) - \pi\right)\right) \end{aligned}$$

Trigonometric identities together with the property  $P_l^0(-x) = (-1)^l P_l^0(x)$  allow us to redefine

$$\begin{aligned} s^-(\omega, r) &= \sin\left(\sin^{-1}\left(\frac{r \sin \omega}{R}\right) - \omega\right) \\ P_l^-(\omega, r) &= P_l^0\left(\cos\left(\sin^{-1}\left(\frac{r \sin \omega}{R}\right) - \omega\right)\right) \\ s^+(\omega, r) &= -\sin\left(\sin^{-1}\left(\frac{r \sin \omega}{R}\right) + \omega\right) \\ P_l^+(\omega, r) &= (-1)^l P_l^0\left(\cos\left(\sin^{-1}\left(\frac{r \sin \omega}{R}\right) + \omega\right)\right). \end{aligned}$$

Therefore, equation (12) may be written as

$$(\mathcal{R}_{\mathcal{T}}f)_{lm}(\omega) = \frac{2\pi}{\sin \omega} \int_R^{\frac{R}{\sin \omega}} dr r f_{lm}(r) \frac{1}{\sqrt{\left(\frac{R}{\sin \omega}\right)^2 - r^2}} [s^-(\omega, r) P_l^-(\omega, r) - s^+(\omega, r) P_l^+(\omega, r)].$$

Finally, we get

$$(\mathcal{R}_{\mathcal{T}}f)_{lm}(\omega) = \int_R^{\frac{R}{\sin \omega}} dr f_{lm}(r) \frac{1}{\sqrt{\left(\frac{R}{\sin \omega}\right)^2 - r^2}} \times$$



$$\frac{2\pi}{\sin \omega} \sum_{\sigma=\pm 1} \frac{r \sin \left( \sin^{-1} \left( \frac{r \sin \omega}{R} \right) - \sigma \omega \right)}{\sqrt{\left( \frac{R}{\sin \omega} \right) + r}} (\sigma)^l P_l^0 \left( \cos \left( \omega - \sigma \sin^{-1} \left( \frac{r \sin \omega}{R} \right) \right) \right), \quad (19)$$

The support of function  $f_{lm}(r)$  enables to change the lower integration limit  $R$  by  $r_m$ . Making the substitution  $p = R/\sin \omega \ddagger$  and keeping the notation for readability§, the integral equation is:

$$\begin{aligned} (\mathcal{R}_{\mathcal{T}}f)_{lm}(p) &= \int_{r_m}^p dr f_{lm}(r) \frac{1}{\sqrt{p-r}} \times \\ &\frac{2\pi}{R} \sum_{\sigma=\pm 1} \sigma^l \frac{p r \sin \left( \sin^{-1} \left( \frac{r}{p} \right) - \sigma \sin^{-1} \left( \frac{R}{p} \right) \right)}{\sqrt{p+r}} P_l^0 \left( \cos \left( \sin^{-1} \left( \frac{R}{p} \right) - \sigma \sin^{-1} \left( \frac{r}{p} \right) \right) \right). \end{aligned} \quad (20)$$

Then, we have

$$(\mathcal{R}_{\mathcal{T}}f)_{lm}(p) = \int_{r_m}^p dr f_{lm}(r) \frac{1}{\sqrt{p-r}} K_l(p, r), \quad (21)$$

and the kernel is

$$K_l(p, r) = \frac{2\pi}{R} \sum_{\sigma=\pm 1} \sigma^l \frac{p r \sin \left( \sin^{-1} \left( \frac{r}{p} \right) - \sigma \sin^{-1} \left( \frac{R}{p} \right) \right)}{\sqrt{p+r}} P_l^0 \left( \cos \left( \sin^{-1} \left( \frac{R}{p} \right) - \sigma \sin^{-1} \left( \frac{r}{p} \right) \right) \right) \quad (22)$$

and it may also be written as

$$K_l(p, r) = \frac{2\pi}{R} \sum_{\sigma=\pm 1} \sigma^l \frac{r^2 \sqrt{p^2 - R^2} - \sigma R r \sqrt{p+r} \sqrt{p-r}}{p \sqrt{p+r}} P_l^0 \left( \frac{\sqrt{p^2 - R^2} \sqrt{p+r} \sqrt{p-r} + \sigma R r}{p^2} \right). \quad (23)$$

The kernel (23) is suitable for the evaluation of the existence of a unique solution of (12) according to theorem 4.1. For clarity of notation, we use the abbreviation  $P(\cdot) = P_l^0(\cdot)$ . We define  $\Delta(r_m, r_M) := \{r_m \leq r \leq p \leq r_M\}$  and show that the assumptions (i)-(iii) are verified.

(i)  $K_l \in C^3(\Delta(a, b))$ :

The kernel (23) is smooth in  $\Delta(r_m, r_M)$ . Notice that it is smooth on the diagonal  $p = r$  because it is an even polynomial in  $\sqrt{p-r}$ , i.e.  $Q(\sqrt{p-r}) = Q(-\sqrt{p-r})$ .

Thus, assumption (i) is verified.

‡ Physically  $p$  is the diameter of the circles that generate the torus as a surface of revolution.

§ Strictly speaking, we should have changed the function after this substitution, for instance  $(\mathcal{R}_{\mathcal{T}}f)_{lm}(\sin^{-1} R/p) = (\widetilde{\mathcal{R}}_{\mathcal{T}}f)_{lm}(p)$ .

(ii)  $N_{K_l} := \{r \in [r_m, r_M] | K_l(r, r) = 0\}$  is finite and consists of simple roots:

For  $r = p$  the kernel is

$$K_l(r, r) = \frac{\sqrt{8\pi}}{R} \sqrt{r} \sqrt{r^2 - R^2} P\left(\frac{R}{r}\right).$$

Since  $0 < R < r_m \leq r$ , the factors accompanying  $P$  never vanish and  $K_l(r, r)$  has the same zeros as  $P\left(\frac{R}{r}\right)$ . Given that  $P$  is an orthogonal polynomial,  $P\left(\frac{R}{r}\right)$  has a finite number of simple roots as well as the kernel.

(iii) For every  $r \in N_{K_l}$ , the gradient  $(\beta_1, \beta_2) = \nabla K_l(r, r)$  satisfies

$$1 + \frac{1}{2} \frac{\beta_1}{\beta_1 + \beta_2} > 0.$$

Note that we cannot differentiate the kernel straightforwardly to obtain  $\frac{\partial K_l}{\partial r}(p, r)$  and  $\frac{\partial K_l}{\partial p}(p, r)$ . We define a function  $w : [r_m, r_M] \rightarrow [r_m, r_M] \times [r_m, r_M]$  such that  $w(r) = (r, r)$  and defining the composition  $v(r) = (K_l \circ w)(r)$ , then  $v'(r) = \frac{\partial K_l}{\partial p}(r, r) + \frac{\partial K_l}{\partial r}(r, r) = \beta_1 + \beta_2$ .

On the other hand, since

$$v(r) = \frac{\sqrt{8\pi}}{R} \sqrt{r} \sqrt{r^2 - R^2} P\left(\frac{R}{r}\right)$$

its derivative at the zeros  $r_0$  of the kernel is

$$v'(r_0) = -\frac{\sqrt{8\pi}}{r_0^2} \sqrt{r_0^3 - R^2 r_0} P'\left(\frac{R}{r_0}\right) = \beta_1 + \beta_2.$$

To evaluate  $\beta_2$  we write the kernel as a power expansion around  $r = r_0$

$$K_l(r_0, r_0 - \varepsilon) = K_l(r_0, r_0) + \frac{\partial K_l}{\partial r}(r_0, r_0)(-\varepsilon) + \frac{1}{2} \frac{\partial^2 K_l}{\partial r^2}(r_0, r_0)\varepsilon^2 + \dots$$

where  $r_0$  is a zero of  $K_l(r, r)$ . The factor multiplying  $(-\varepsilon)$  in the expansion is the second component  $\beta_2 = \frac{\partial K_l}{\partial r}(r_0, r_0)$  in the gradient. We write a power series representation of the kernel (23) according

$$\begin{aligned} K_l(r_0, r_0 - \varepsilon) &= \frac{2\pi}{R} \sum_{\sigma=\pm 1} \sigma^l \frac{(r_0 - \varepsilon)^2 \sqrt{r_0^2 - R^2} - \sigma R(r_0 - \varepsilon) \sqrt{2r_0 - \varepsilon} \sqrt{\varepsilon}}{r_0 \sqrt{2r_0 - \varepsilon}} \times \\ &\quad P\left(\frac{\sqrt{r_0^2 - R^2} \sqrt{2r_0 - \varepsilon} \sqrt{\varepsilon} + \sigma R(r_0 - \varepsilon)}{r_0^2}\right) \\ &= \frac{2\pi}{R} \sum_{\sigma=\pm 1} \sigma^l \left[ \sqrt{\frac{r_0}{2}} \sqrt{r_0^2 - R^2} - \sigma R \sqrt{\varepsilon} + J(\varepsilon) \right] \times \\ &\quad \left[ \sqrt{2r_0} \frac{\sqrt{r_0^2 - R^2}}{r_0^2} P'\left(\frac{\sigma R}{r_0}\right) \sqrt{\varepsilon} + \left( 2 \frac{r_0^2 - R^2}{r_0^3} P''\left(\frac{\sigma R}{r_0}\right) - 2 \frac{\sigma R}{r_0^2} P'\left(\frac{\sigma R}{r_0}\right) \right) \varepsilon + J(\varepsilon^{3/2}) \right] \end{aligned}$$

where terms in brackets  $[\cdot]$  are the power expansions of the corresponding factors and  $J(\varepsilon^d)$  means a linear combination integer and half-integer powers of  $\varepsilon$  equal or higher than  $d$ , i.e.

$$J(\varepsilon^d) = a\varepsilon^d + b\varepsilon^{d+1/2} + c\varepsilon^{d+1} + \dots$$

We use the symmetry properties  $P''(-x) = (-1)^l P''(x)$  and  $P'(-x) = (-1)^{l+1} P'(x)$  and the identity  $(1-x^2)P''(x) - 2xP'(x) + l(l+1)P(x) = 0$  to get

$$P''\left(\frac{R}{r_0}\right) = \frac{2Rr_0}{r_0^2 - R^2} P'\left(\frac{R}{r_0}\right).$$

Then, the factor multiplying  $(-\varepsilon)$  in the series expansion is  $\beta_2 = 0$  and we get the ratio

$$1 + \frac{1}{2} \frac{\beta_1}{\beta_1 + \beta_2} = 3/2 > 0,$$

as we wanted to show.

#### 4.1. Invertibility

We proved that the assumptions (i), (ii) and (iii) of Theorem 4.1 are fulfilled by the kernel  $K_l(p, r)$ . So, the radial components  $f_{lm}(r)$  of function  $f$  can be recovered uniquely from the coefficients of the expansion of data

$$\mathcal{R}_{\mathcal{T}}f(p, \alpha, \beta) = \sum_{l \in \mathbb{N}} \sum_{|m| \leq l} (\mathcal{R}_{\mathcal{T}}f)_{lm}(p) Y_l^m(\beta, \alpha).$$

Notice that here we have expressed data in terms of the diameter  $p$  instead of the scattering angle  $\omega$ . See section 5.1 for the explicit definition of  $\mathcal{R}_{\mathcal{T}}f(p, \alpha, \beta)$ .

**Corollary 4.1.** *(Invertibility of the  $\mathcal{R}_{\mathcal{T}}f$ )* If  $f_1$  and  $f_2$  are in  $C^\infty(S_h(r_m, r_M))$  and  $\mathcal{R}_{\mathcal{T}}f_1 = \mathcal{R}_{\mathcal{T}}f_2$ , then  $f_1 = f_2$ .

*Proof.* Let  $f$  satisfy  $(\mathcal{R}_{\mathcal{T}}f)_{lm} = 0$  for all  $l, m$  in the spherical harmonic expansion. According Theorem 4.1, there is a unique solution  $f_{lm} = 0$ , which implies  $f = 0$ . The linearity of  $\mathcal{R}_{\mathcal{T}}f$  yields the claim.  $\square$

The previous result is also useful to stress an additional fact.

**Theorem 4.2.** *Let  $f \in C^\infty(S_h(r_m, r_M))$ . Then,  $(\mathcal{R}_{\mathcal{T}}f)_{lm}(p)$  in the range  $p \in [r_m, r_0]$  with  $r_0 \leq r_M$  determines uniquely  $f_{lm}(r)$  in the range  $r \in [r_m, r_0]$ .*

*Proof.* The claim follows from theorem 4.1 applied in the domain  $\Delta(r_m, r_0) := \{r_m \leq r \leq p \leq r_0\}$ , where the assumptions (i)-(iii) on the kernel hold, and from corollary 4.1.  $\square$

**Remark 4.1.** *A hole theorem. The toric Radon transform  $\mathcal{R}_{\mathcal{T}}f(p, \alpha, \beta)$  of a compact supported function is not compact supported. However, Theorem 4.2 states that  $f$  is uniquely determined by the limited set of data consisting on integrals on the tori with diameter  $p \leq r_M$ . This claim resembles the well-known hole theorem for the Radon transform on circles discussed in [6], where an explicit formula shows that the original function is uniquely determined by integrals on circles with bounded diameters.*

**Remark 4.2.** *The scope of Remark 4.1 is theoretical since in numerical implementations some issues on stability and artifacts may arise when attempting to recover the function from a highly restricted data set.*

**Remark 4.3.** *The singular support of the function can alternatively be recovered from the toric data using a filtered-backprojection approach [17]. Tori (1) are a particular case of those parametrized there ([17], equation 3). Then, the contour reconstruction framework developed for the four configurations introduced there is suitable for this modality.*

## 5. Numerical Simulations

Provided that the invertibility of our toric Radon transform has been proved we can by-pass the lack of inverse formula using a numerical inversion method. In such case, a matrix formulation of the problem, i.e.  $A\mathbf{f} = \mathbf{g}$ , may be used. Several methods are suitable for this purpose. Particularly, Tikhonov regularization requires to solve a set of normal equations where a regularization parameter is set. In order to do so, we use an approach based on the discrete spherical harmonic expansion of the functions representing the data and the object.

### 5.1. Forward model

An alternative definition of our toric Radon transform useful in numerical simulation is

$$\mathcal{R}_{\mathcal{T}}f(p, \alpha, \beta) = p^2 \int_0^\pi d\gamma \int_0^{2\pi} d\psi \cos\left(\gamma - \cos^{-1} \frac{R}{p}\right) \sin \gamma f\left(\Phi^{p,\alpha,\beta}(\gamma, \psi)\right), \quad (24)$$

where  $p \in (R, +\infty)$  is the diameter of the circles making the torus and

$$\Phi^{p,\alpha,\beta}(\gamma, \psi) = r\Theta^{\alpha,\beta}(\gamma, \psi)|_{r=p \cos(\gamma - \cos^{-1} \frac{R}{p})} \quad (25)$$

is the parametrization of the toric surface labeled by variables  $(p, \alpha, \beta)$ . The unit vector  $\Theta^{\alpha,\beta}(\gamma, \psi)$  was introduced in the definition (1). The scattering angle  $\omega$  and the diameter  $p$  are related through  $p = R/\sin \omega$ .

### 5.2. The algebraic problem

In this section we use the discrete spherical harmonic expansion of the data and the object to write it as an algebraic problem suitable for Tikhonov regularization. This is achieved using numerical algorithms for the Discrete-Inverse Spherical Harmonic

transform (DSHT-IDSHT), see Appendix A for a description of the algorithms. The pair DSHT-IDSHT allows to write the problem in the domain of the spherical harmonics according

$$\mathbf{g}_{nk}^j \underset{\text{IDSHT}}{\overset{\text{DSHT}}{\rightleftharpoons}} \mathbf{g}_{lm}^j \quad (26)$$

$$\mathbf{f}_{nk}^i \underset{\text{IDSHT}}{\overset{\text{DSHT}}{\rightleftharpoons}} \mathbf{f}_{lm}^i \quad (27)$$

where the discrete functions are  $\mathbf{g}_{nk}^j = \mathcal{R}_{\mathcal{T}}f(p_j, \alpha_n, \beta_k)$ ,  $\mathbf{g}_{lm}^j = (\mathcal{R}_{\mathcal{T}}f)_{lm}(p_j)$  with  $j = 0, \dots, N_p - 1$ ,  $\mathbf{f}_{nk}^i = f(r_i \cos \psi_n \sin \gamma_k, r_i \sin \psi_n \sin \gamma_k, r_i \cos \gamma_k)$  and  $\mathbf{f}_{lm}^i = f_{lm}(r_i)$  with  $i = 0, \dots, N_r - 1$ . In this domain, the components of the vector representing the unknown function  $\mathbf{f}_{lm}$  are related to components of the vector for the known data  $\mathbf{g}_{lm}$  through the equation  $\mathbf{g}_{lm} = A_l \mathbf{f}_{lm}$  that is the algebraic relative of equation (21). This algebraic problem must be solved for each combination  $l, m$ .

### 5.3. Matrix generation

Matrix  $A_l \in \mathbb{R}^{N_p \times N_r}$  is the key for solving the numerical inverse problem. Given that the kernel in (21) is  $l$ -dependent and  $m$ -independent, only  $N+1$  matrices may be generated. Here we explain how to approximate it adopting the convention  $N_p = N_r = M$ . Splitting up the integration range in equation (21) and rewriting

$$(\mathcal{R}_{\mathcal{T}}f)_{lm}(p_j) = \sum_{q=0}^{M-1} \int_{r_q}^{r_{q+1}} dr f_{lm}(r) \frac{r}{\sqrt{p_j^2 - r^2}} \tilde{K}_l(p_j, r) \quad (28)$$

where  $r_q = r_m + q(p_j - r_m)/M$  and  $\tilde{K}_l(p_j, r) = \sqrt{p_j + r} K_l(p_j, r)/r$ . Then, assuming that  $\tilde{K}_l(p_j, r)$  is constant in the interval  $[r_q, r_{q+1}]$  we can approximate it with its value in the midpoint  $r_q := (q + 1/2)/M$  and the discrete form for the equation is

$$\mathbf{g}_{lm}^j = (\mathcal{R}_{\mathcal{T}}f)_{lm}(p_j) \simeq \sum_{q=j}^{M-1} w_{j,q} \tilde{K}_l(p_j, r_q) f_{lm}(r_q), \quad (29)$$

with the analytically calculated weighting factor

$$w_{j,q} := \int_{r_q}^{r_{q+1}} dr \frac{r}{\sqrt{p_j^2 - r^2}}. \quad (30)$$

Finally, the entries of the matrix in equation  $\mathbf{g}_{lm} = A_l \mathbf{f}_{lm}$  are

$$A_l = \left( w_{j,q} \tilde{K}_l(p_j, r_q) \right)_{j,q=0 \dots M-1} \in \mathbb{R}^{M \times M}. \quad (31)$$

**Table 1.** Sketch of the reconstruction algorithm.

Matrix $A_l$ is precalculated with the middle point method.
1: Chose a suitable value for $\lambda$ according to signal conditions
2: Perform DSHT (26) to data $\mathbf{g}_{nk}^j$ to obtain $\mathbf{g}_{lm}^j$
3: For each pair $l, m$ : weight data using the window function $\mathbf{w}_{lm}$
4: For each pair $l, m$ : solve the normal equations in (32) and obtain an approximation of $\mathbf{f}_{lm}^i$
5: Perform IDSHT (27) to obtain the reconstruction $\mathbf{f}_{nk}^i$
6: Interpolate to obtain the function in discrete Cartesian coordinates $\tilde{\mathbf{f}}$

#### 5.4. Overview of the reconstruction algorithm

The reconstruction strategy is based on the implementations of the algorithms for discrete spherical harmonic expansion described in Appendix A for data as well as for the sought function according to equations (26) and (27). The algorithm is summarized in Table 1 and is aimed to solve the matrix problem  $\mathbf{g}_{lm} = A_l \mathbf{f}_{lm}$  for  $l = 0, \dots, N$  and  $|m| \leq l$ . Tikhonov regularization requires to solve the normal equations

$$(A_l^T A_l + \lambda I) \mathbf{f}_{lm} = A_l^T \mathbf{g}_{lm} \quad (32)$$

where  $I$  is the identity matrix and  $\lambda$  is a regularization parameter. When the same range and discretization is chosen for  $r$  and  $p$  matrix  $A_l$  is triangular and normal equations can be easily solved by forward substitution. In order to compensate the effects of discretization, i.e. finite order in the spherical harmonic expansion and finite maximal diameter of tori ( $p_M$ ), we weight data with the following windowing function  $\mathbf{w}_{lm}$  whose components are defined as

$$w_{lm}^j = \frac{W_l W_m}{\sqrt{2}-1} \left[ \frac{\sqrt{2}}{\sqrt{1 + \left(\frac{p_j - R}{p_M - R}\right)^{1.7}}} - 1 \right], \quad (33)$$

where the filters  $W_l$  and  $W_m$  are defined in (A.11) and (A.12).

#### 5.5. Results

Data was simulated using equation (24), a system where detector moves on a sphere of radius  $R = 1/8$  was considered. The object was a 3D Shepp-Logan phantom of size  $64 \times 64 \times 64$ , see figure 3. The function was supported in a cube of side  $L = 1$  in the first octant with coordinate  $(x_{\min}, y_{\min}, z_{\min}) = (L/64, L/64, R)$ . Discretization parameters of data are:  $N_\alpha = 513$ ,  $N_\beta = 256$  and  $N_p = 256$ . The maximal diameter of the circles making the torus is  $p_M = 4r_M$  where  $[r_m, r_M]$  is the radial support of the cube containing the phantom. Numerical integration is performed in variables  $\gamma$  and  $\psi$  with  $\Delta\psi = 2\pi/N_\psi$  and the variable step  $\Delta\gamma = \cos^{-1}(p/R)/N_\gamma$ , with  $N_\gamma = 256$  and  $N_\psi = 256$ . Figure 4 shows simulated data for different values of angle  $\alpha$ . The trapezoidal

rule was used to perform numerical integration. According to the discretization chosen for data, the order of the spherical harmonic expansion was  $N = 256$  ( $N_\alpha = 2N + 1$ , see Appendix A). Data were also corrupted with Gaussian noise with several signal to noise ratios. In order to asses the quality of reconstruction we used the following measures of error: the Normalized Mean Square Error (%)

$$\text{NMSE} = \frac{100}{N^3} \frac{\|\mathbf{f} - \tilde{\mathbf{f}}\|_2^2}{\max_i \{\mathbf{f}_i^2\}} \quad (34)$$

and the Normalized Mean Absolute Error (%)

$$\text{NASE} = \frac{100}{N^3} \frac{\|\mathbf{f} - \tilde{\mathbf{f}}\|_1}{\max_i \{\mathbf{f}_i\}}, \quad (35)$$

where  $\mathbf{f}$  is the original image and  $\tilde{\mathbf{f}}$  is the reconstruction. Reconstructions (algorithm in Table 1) were carried out for two values of lambda:  $\lambda = 0.05$  (noiseless data) and  $\lambda = 0.1$  (noisy data) chosen in an heuristic fashion. The same values were used for the a given set of normal equations (32). Figure 5 shows reconstructions for noiseless data and figures 6 to 8 show reconstructions from corrupted data. The original function as well as reconstructions are shown at planes  $z=10, 11, 12, 15, 18, 20, 25, 26, 29, 32, 35, 36, 41, 44, 46, 49, 52$  and  $53$  from top to bottom and from left to right. No post processing was applied to images. Error metrics are displayed in figure captions.

## 6. Discussion

In section 4 we presented our most relevant finding: the fact that the spherical harmonic components of the function can be uniquely recovered from the spherical harmonic components of data. The immediate consequence of that is the invertibility of the toric Radon transform. Numerical simulations in section 5 illustrate this fact. In average, reconstructions exhibit acceptable quality: objects inside are distinguished, shapes are kept and error metrics seem to be reasonable. As expected, stronger regularization is required for noisy data. Some artifacts and loss of contrast suggest the need of further progress in the reconstruction technique. Images may be enhanced by an optimization strategy such as the choice of best regularization parameters in the  $L$ -curve [24]. In addition, more advanced regularization techniques like iterative approaches for Tikhonov [25] or variational [26] regularization may improve reconstructions.

Our reconstruction approach in the domain of discrete spherical harmonics allows splitting up the problem reducing the size of the matrices with respect with a standard algebraic treatment. With the same discretization we may have needed a  $N_\alpha N_\beta N_p \times N^3$  matrix (more than  $4.10^{12}$  entries) whereas we used a set of  $N + 1 = 257$  matrices of size  $M \times M$  ( $M = 128$ ). Recently, reconstruction methods based on deep learning have achieved promising performance in conventional x-ray scanning, sparse view and compressed sensing applications [27, 28, 29]. In a deep learning reconstruction strategy, dimension reduction by means of discrete spherical harmonic expansion may enable

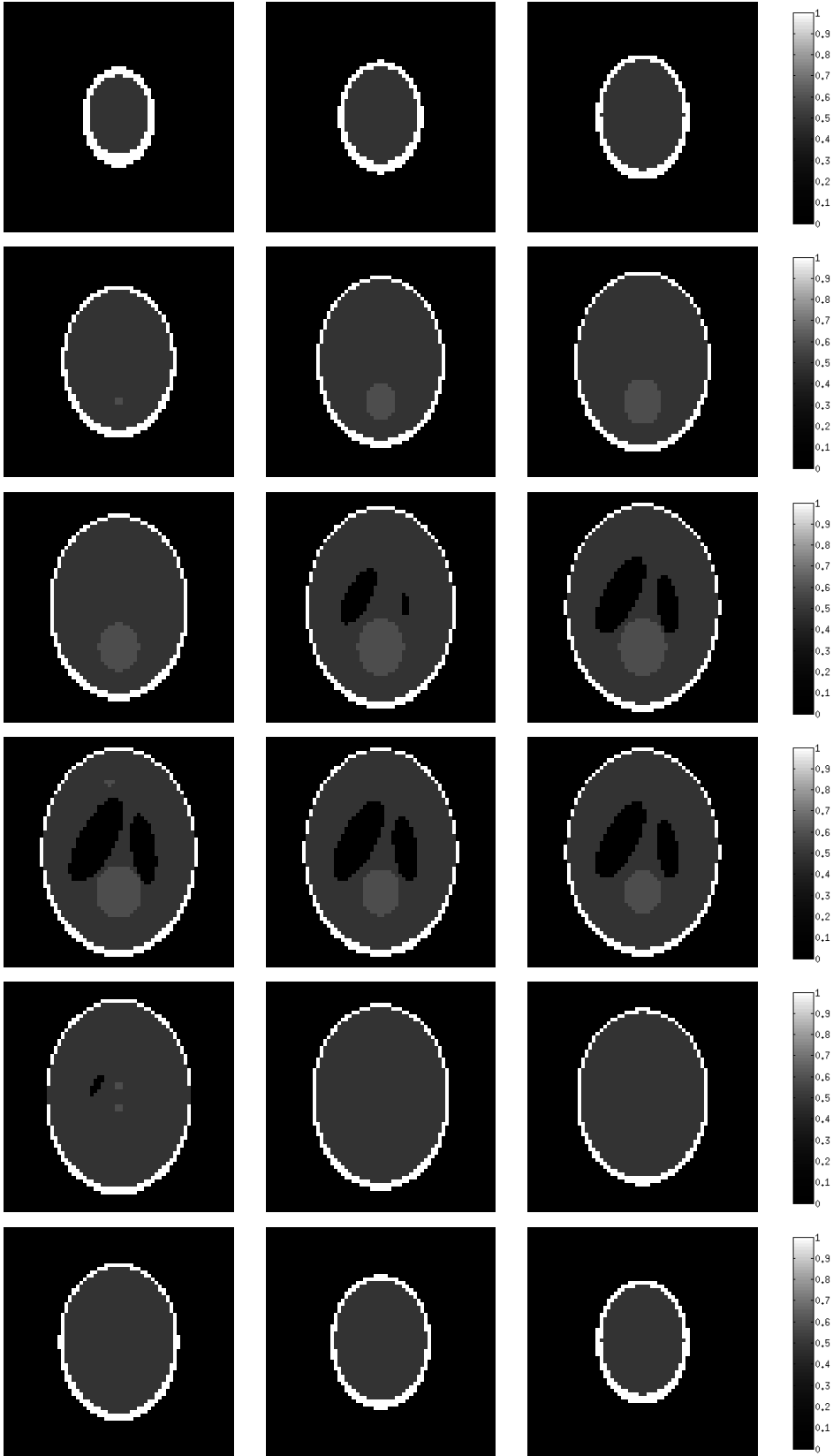
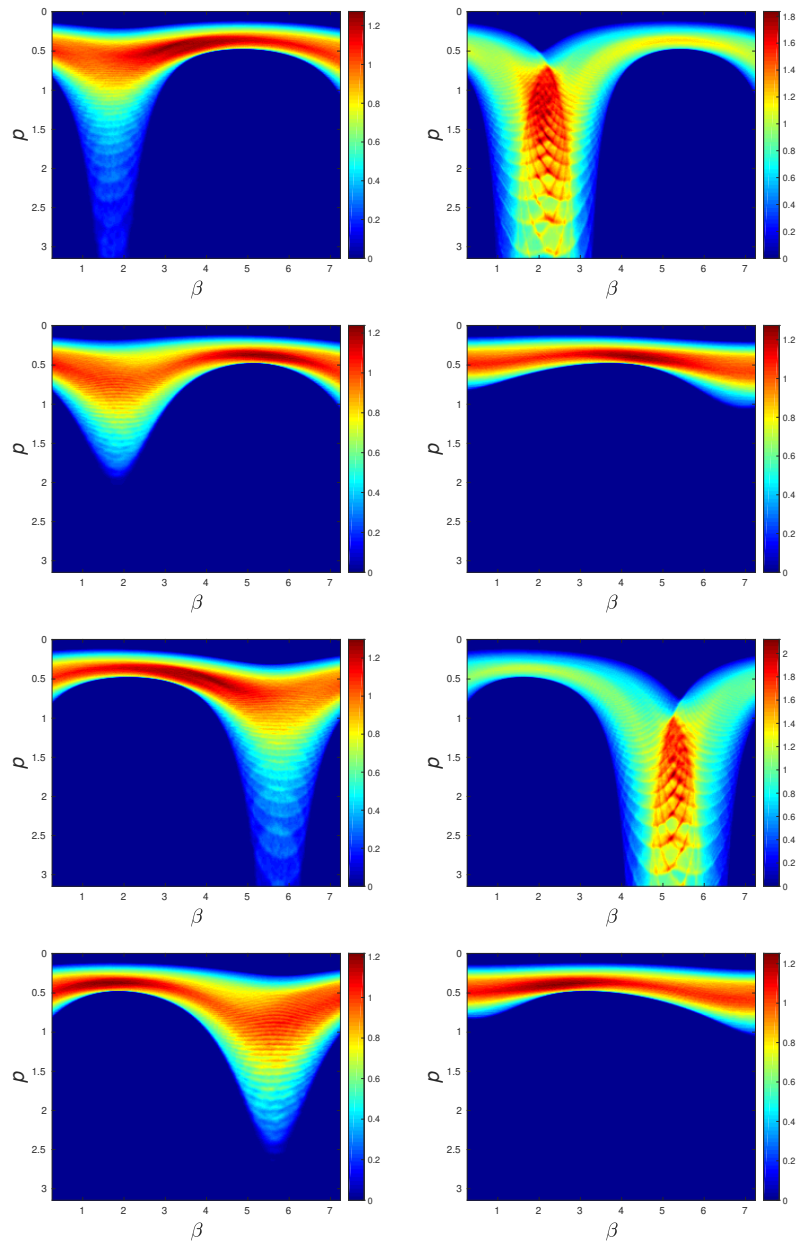


Figure 3. Original 3D phantom used for simulations.





**Figure 4.** Data simulated using (24). Function  $\mathcal{R}_T(p, \alpha, \beta)$  is shown for the sets  $\alpha = 0, \pi/4, \pi/2, 3\pi/4, \pi, 5\pi/4, 3\pi/2, 7\pi/4$ .

to reduce the input and output layers or neural networks and, thus, the size of the underlying architecture. From a theoretical point of view, this may turn feasible to obtain efficient and high quality reconstructions from compressed Compton scattering data. This encourages future work on the topic since compressed sensing, i.e. registering few energies, may enable faster scanning increasing the potential of this configuration. Nevertheless, progress in deep learning is quite recent and extra effort should be done in order to ensure reliable algorithms.

Regarding the novel setup for Compton scatter tomography, the geometry offers some

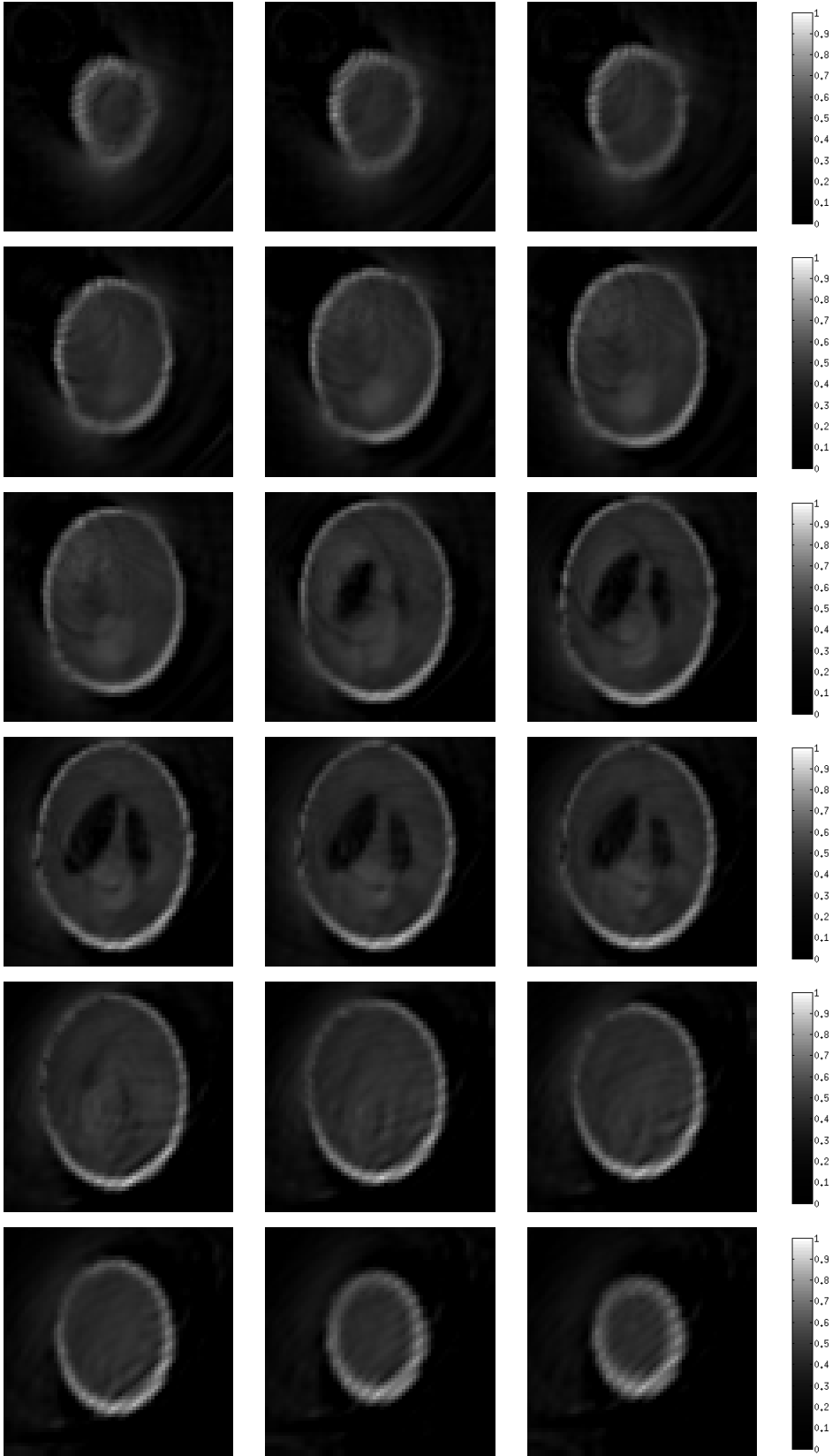


**Figure 5.** Reconstructions from noiseless data ( $\lambda = 0.05$ ). Errors are NMSE=1.92 % (NMAE=6.16 %).

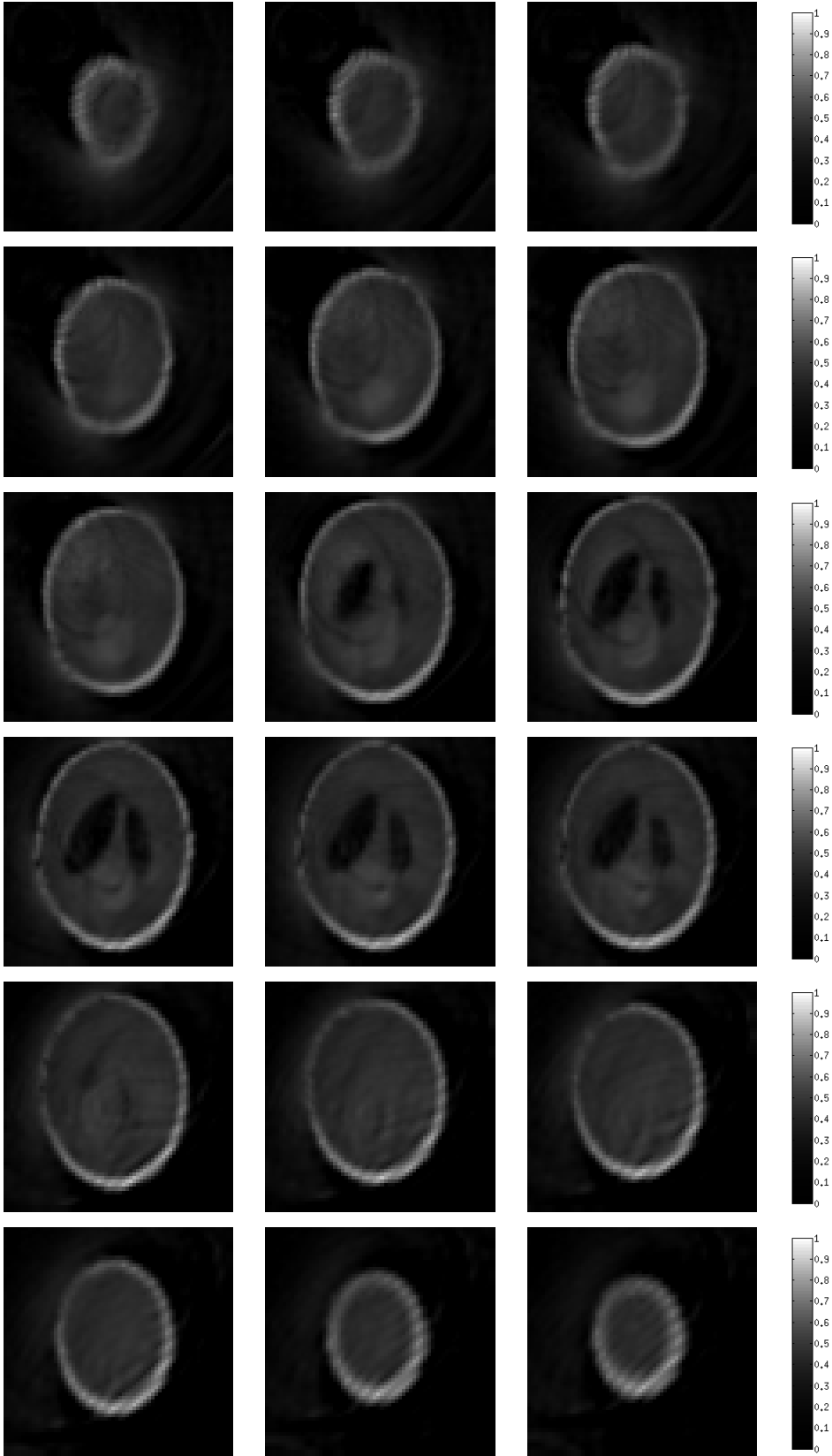


**Figure 6.** Reconstructions from noisy data with SNR=30 dB ( $\lambda = 0.1$ ). Errors are NMSE=1.93 % (NMAE=6.06 %).

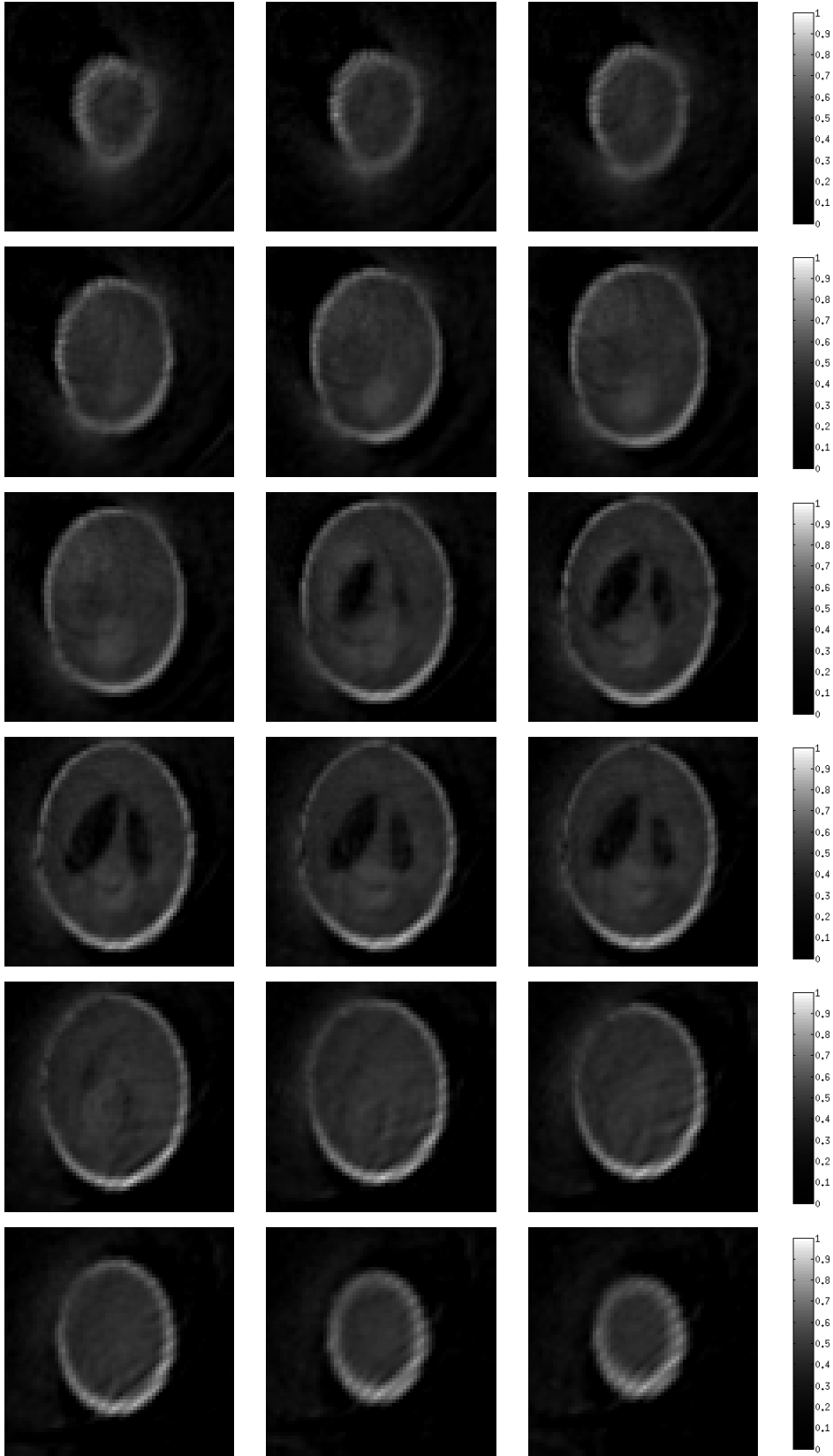


**Figure 7.** Reconstructions from noisy data with SNR=20 dB ( $\lambda = 0.1$ ). Errors are NMSE=1.93 % (NMAE=6.10 %).

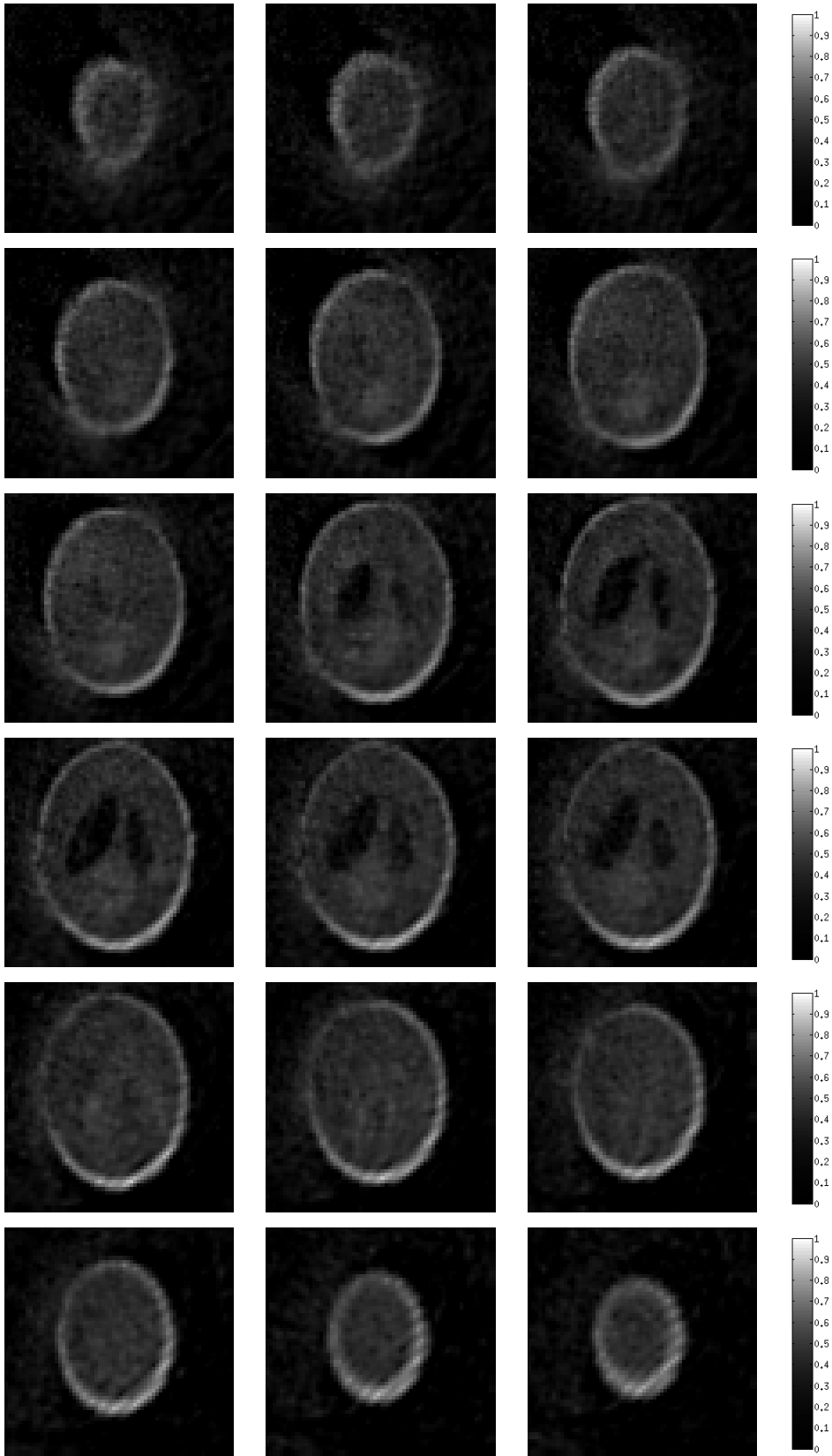


**Figure 8.** Reconstructions from noisy data with SNR=10 dB ( $\lambda = 0.1$ ). Errors are NMSE=1.98 % (NMAE=6.47 %).

material advantages like using one single detector and a non-moving uncollimated source. This may be an advantageous in scenarios where relative movement between the source and the object is difficult to accomplish.

## 7. Conclusion

We introduced a novel Compton scatter tomography in three dimensions that has some potential advantages in front to other designs. Measured data is modeled by a toric Radon transform. We demonstrated the invertibility of the toric transform by proving the uniqueness of the solutions of the one dimensional Abel's type equation resulting from its spherical harmonic expansion. In addition, we developed a reconstruction method based on the discrete spherical harmonic expansion and Tikhonov regularization. Numerical simulations confirm the feasibility of the approach and raise some questions on the improvement of algorithm. The discrete expansion approach may be suitable for more sophisticated regularization and also for deep learning based reconstruction techniques enabling, thus, new implementation advantages. Some studies are on the way.

## Acknowledgements

J. Cebeiro is supported a CONICET postdoctoral grant (# 171800). D. Rubio, J. Cebeiro and M. A. Morvidone are partially supported by SOARD-AFOSR (grant number FA9550-18-1-0523). C. Tarpau research work is supported by grants from Région Ile-de-France (in Mathematics and Innovation) 2018-2021 and LabEx MME-DII (Modèles Mathématiques et Economiques de la Dynamique, de l'Incertitude et des Interactions) (No. ANR-11-LBX-0023-01).

## Appendix A. Discrete Spherical Harmonic Expansion for 3D imaging

In this section we explain the algorithm for numerical calculation of the spherical harmonic expansion of a *band-limited* function in  $\mathbb{R}^3$ . The idea consists in sampling a function on spheres of different radii in order to obtain several functions on the sphere. Finally, the spectral representation of each function is calculated with through a technique based on the algorithms for the Discrete Fourier Transform (DFT-IDFT) and the Discrete Legendre Transform (DLT-IDLT). We call this forward-inverse pair the Discrete Spherical Harmonic Transform (DSHT-IDSHT). The algorithm is based in [30] and its application in [31].

Let  $F$  be a *band-limited* function (i.e.  $F_{lm}(r) = 0 \forall l > N$ ) supported in the space between the balls  $B_{r_{\max}}(0)$  and  $B_{r_{\min}}(0)$  such that

$$F(r, \theta, \varphi) = \sum_{l=0}^N \sum_{|m| \leq l} F_{lm}(r) q_l^m P_l^m(\cos \theta) e^{im\varphi}, \quad (\text{A.1})$$

or equivalently

$$F(r, \theta, \varphi) = \sum_{m=-N}^N \sum_{l=|m|}^N F_{lm}(r) q_l^m P_l^m(\cos \theta) e^{im\varphi}, \quad (\text{A.2})$$

where  $m = -N, \dots, N$  and  $l = |m|, \dots, N$ ,  $P_l^m(\cdot)$  are the associated Legendre polynomials and  $q_l^m$  are the normalization coefficients [21] defined as

$$q_l^m = (-1)^m \sqrt{\frac{2l+1}{4\pi} \frac{(l-m)!}{(l+m)!}}. \quad (\text{A.3})$$

Let's consider the following discretization parameters  $\Delta r = (r_{\max} - r_{\min})/(N_r - 1)$  and  $\Delta\varphi = 2\pi/(2N + 1)$  and their corresponding indices  $j = 0, \dots, N_r - 1$  and  $n = -N, \dots, N$ . Discrete values of variables for radial and azimuthal variables are  $r_j = j\Delta r + r_{\min}$  and  $\varphi_n = 2\pi n/(2N + 1)$ . Latitude variable  $\theta$  is arbitrarily sampled<sup>||</sup> in the interval  $[0, \pi]$  and is labeled  $\theta_k$ ,  $k = 1, \dots, N_\theta$ .

Using this sampling, function (A.2) is

$$F(r_j, \theta_k, \varphi_n) = \mathbf{F}_{kn}^j = \sum_{m=-N}^N \widehat{\mathbf{F}}_{km}^j e^{im\varphi_n}, \quad (\text{A.4})$$

with

$$F_m(r_j, t_k) = \widehat{\mathbf{F}}_{km}^j = \sum_{l=|m|}^N \mathbf{F}_{lm}^j q_l^m P_l^m(t_k), \quad (\text{A.5})$$

where  $\mathbf{F}_{lm}^j = F_{lm}(r_j)$ ,  $t_k = \cos(\theta_k)$  ( $t = \cos \theta$ ) and coefficients  $F_{lm}(r_j)$  are evaluated thanks to the orthogonality properties of the associated Legendre polynomials according

$$F_{lm}(r_j) = \int_{-1}^1 dt F_m(r_j, t) q_l^m P_l^m(t) \approx \sum_{k=1}^{N_\theta} F_m(r_j, t_k) q_l^m P_l^m(t_k) w_k, \quad (\text{A.6})$$

where  $w_k$  are the Gaussian curvature coefficients<sup>¶</sup>.

Now, we recall the definitions forward-inverse pairs for the Discrete Fourier Transform (DFT-IDFT)

$$\mathbf{X}_m = \text{DFT} \{ \mathbf{x}_n \} = \sum_{n=-N}^N \mathbf{x}_n e^{-i2\pi nm/(2N+1)} \quad (\text{A.7})$$

where  $\mathbf{x}_n$  ( $n = -N, \dots, N$ ) is a  $2N + 1$  points sequence and  $\mathbf{X}_m$  ( $m = -N, \dots, N$ ) is its  $2N + 1$  points DFT. The inverse is defined as

$$\mathbf{x}_n = \text{IDFT} \{ \mathbf{X}_m \} = \frac{1}{N} \sum_{m=0}^{N-1} \mathbf{X}_m e^{i2\pi nm/(2N+1)}. \quad (\text{A.8})$$

<sup>||</sup> i.e. not necessarily uniformly.

<sup>¶</sup> In particular, using uniform discretization in variable  $\Delta\theta = \pi/N_\theta$  so that  $\theta_k = k\pi/N_\theta$  we have  $F_{lm}(r_j) \approx \sum_{k=1}^{N_\theta} F_m(r_j, \cos \theta_k) q_l^m P_l^m(\cos \theta_k) \sin \theta_k$ .

For a fixed  $m$ , the associated Discrete Legendre Transform pairs (DLT-IDLT) are

$$\mathbf{Y}_{km} = \text{DLT}^m \{ \mathbf{y}_l \} = \sum_{l=|m|}^N \mathbf{y}_l q_l^m P_l^m(t_k), \quad (\text{A.9})$$

and

$$\mathbf{y}_l = \text{IDLT}^m \{ \mathbf{Y}_{km} \} = \sum_{k=1}^{N_\theta} \mathbf{Y}_{km} q_l^m P_l^m(t_k) w_k, \quad (\text{A.10})$$

where  $l = |m|, \dots, N$ ,  $k = 1, \dots, N_\theta$ .

In equations (A.5) and (A.6) we identify definitions (A.9) and (A.10) while (A.4) is  $N \times \text{IDFT} \left\{ \widehat{\mathbf{F}}_{jkm} \right\}$  if we take into account the discretization  $\varphi_n$ . The relationship between all this representations is summarized in the diagram:

$$\left\{ \mathbf{F}_{kn}^j \right\} \begin{array}{c} \xrightarrow{\frac{1}{N} \cdot \text{DFT}} \\ \xleftrightarrow{N \cdot \text{IDFT}} \end{array} \left\{ \widehat{\mathbf{F}}_{km}^j \right\} \begin{array}{c} \xrightarrow{\text{IDLT}} \\ \xleftrightarrow{\text{DLT}} \end{array} \left\{ \mathbf{F}_{lm}^j \right\}$$

or equivalently

$$\mathbf{F}_{nk}^j \begin{array}{c} \xrightarrow{\text{DSHT}} \\ \xleftrightarrow{\text{IDSHT}} \end{array} \mathbf{F}_{lm}^j.$$

So, we obtain the samples of the spherical harmonic expansion  $\mathbf{F}_{lm}^j = F_{lm}(r_j)$  from the samples of function  $\mathbf{F}_{nk}^j = F(r_j, \theta_k, \varphi_n)$ .

The truncation in the finite series may produce Gibbs artifacts that can be alleviated using multiplicative filters  $W_l$  and  $W_m$

$$W_l = \begin{cases} 1.0 & \text{if } l \leq C_l(N_l - |m|) + |m| \\ 3\tau^2 - 2\tau^3 & \text{if } l > C_l(N_l - |m|) + |m| \end{cases}. \quad (\text{A.11})$$

and

$$W_m = \begin{cases} 1.0 & \text{if } |m| \leq C_m N_m \\ 3\tau^2 - 2\tau^3 & \text{if } |m| > C_m N_m \end{cases}. \quad (\text{A.12})$$

where  $C_l = C_m = 1.0$ ,  $N_l = N_m = N$  and  $\tau$  is defined as

$$\tau = \begin{cases} \frac{N-l}{N-|m|} & \text{for } l \\ 1 - |m|/N_m & \text{for } m \end{cases}. \quad (\text{A.13})$$

Thus, the IDSHT algorithm is applied to function  $\{W_l W_m \mathbf{F}_{lm}^j\}$ . An alternative implementation can be found in [21].



## References

- [1] Norton S J 1994 Compton scattering tomography *J. Appl. Phys* **76** 2007–2015
- [2] Cebeiro J, Nguyen M K, Morvidone M A and Noumowé A 2017 New 'improved' Compton scatter tomography modality for investigative imaging of one-sided large objects *Inverse Problems in Science and Engineering* **25** 1676–1696
- [3] Webber J W and Holman S 2019 Microlocal analysis of a spindle transform *Inverse Problems and Imaging* **13** 231 ISSN 1930-8337
- [4] Jones K C, Redler G, Templeton A, Bernard D, Turian J V and Chu J C 2018 Characterization of Compton-scatter imaging with an analytical simulation method *Physics in Medicine & Biology* **63** 025016
- [5] Redler G, Jones K C, Templeton A, Bernard D, Turian J and Chu J C 2018 Compton scatter imaging: A promising modality for image guidance in lung stereotactic body radiation therapy *Medical physics* **45** 1233–1240
- [6] Cormack A M 1981 The Radon transform on a family of curves in the plane *Proceedings of the American Mathematical Society* **83** 325 – 330
- [7] Cormack A M 1982 The Radon transform on a family of curves in the plane *Proceedings of the American Mathematical Society* **86** 293– 298
- [8] Cormack A M 1984 Radon's problem - old and new *SIAM - AMS Proceedings* **14**
- [9] Truong T T and Nguyen M K 2011 Radon transforms on generalized Cormack's curves and a new Compton scatter tomography modality *Inverse Problems* **27**
- [10] Truong T T and Nguyen M K 2011 On new V-line transforms in  $R^2$  and their inversion *Journal of Physics A: Mathematical and Theoretical* **44** 13
- [11] Webber J 2016 X-ray Compton scattering tomography *Inverse Problems in Science and Engineering* **24** 1323–1346
- [12] Norton S J 2019 Compton-scattering tomography with one source and one detector: a simple derivation of the filtered-backprojection solution *Inverse Problems in Science and Engineering* **0** 1–12
- [13] Tarpau C, Cebeiro J, Morvidone M A and Nguyen M K 2019 A new concept of Compton scattering tomography and the development of the corresponding circular Radon transform *IEEE Transactions on Radiation and Plasma Medical Sciences*
- [14] Tarpau C, Cebeiro J, Nguyen M K, Rollet G and Morvidone M A Accepted may 2020 Analytic inversion of a Radon transform on double circular arcs with applications in Compton scattering tomography *IEEE Transactions on Computational Imaging*
- [15] Webber J W and Lionheart W R B 2018 Three dimensional Compton scattering tomography *Inverse Problems* **34**
- [16] Webber J and Miller E L 2020 Compton scattering tomography in translational geometries *Inverse Problems* **36** 025007
- [17] Rigaud G and Hahn B 2018 3D Compton scattering imaging and contour reconstruction for a class of Radon transforms *Inverse Problems* **34**
- [18] Webber J and Quinto E T 2019 Microlocal analysis of a Compton tomography problem *arXiv preprint arXiv:1902.09623*
- [19] Webber J W and Holman S 2019 Microlocal analysis of a spindle transform *Inverse Problems and Imaging* **13** 231
- [20] Biedenharn L C and Louck J D 1981 *Angular Momentum in Quantum Physics* (Reading, MA, USA: Addison Wesley Publishing Company)
- [21] Driscoll J and Healy D 1994 Computing Fourier transforms and convolutions on the 2-sphere *Advances in Applied Mathematics* **15** 202–250
- [22] Deans S R 2007 *The Radon Transform and Some of Its Applications* (Mineola, New York, USA: Dover Publications)
- [23] Schiefeneder D and Haltmeier M 2017 The Radon transform over cones with vertices on the sphere

- and orthogonal axes *SIAM Journal on Applied Mathematics* **77** 1335–1351
- [24] Hansen P 2001 *Computational Inverse Problems in Electrocardiology* (WIT Press, Southampton, P. Johnston (Ed.)) chap The L-curve and its use in the numerical treatment of inverse problems, pp 119–142
- [25] Gazzola S, Hansen P and Nagy J 2019 IR tools: a MATLAB package of iterative regularization methods and large-scale test problems *Numer Algor* **81** 773–811
- [26] Haltmeier M and Schiefeneder D 2018 Variational regularization of the weighted conical Radon transform *Inverse Problems* **34** 124009
- [27] He J, Wang Y and Ma J 2020 Radon inversion via deep learning *IEEE Transactions on Medical Imaging* 1–1
- [28] Lee H, Lee J, Kim H, Cho B and Cho S 2019 Deep-neural-network-based sinogram synthesis for sparse-view CT image reconstruction *IEEE Transactions on Radiation and Plasma Medical Sciences* **3** 109–119
- [29] Hyun C M, Baek S H, Lee M, Lee S M and Seo J K 2020 Deep learning-based solvability of underdetermined inverse problems in medical imaging (*Preprint* arXiv:arXiv:2001.01432)
- [30] Basko R, Zeng G L and Gullberg G T 1998 Application of spherical harmonics to image reconstruction for the Compton camera *Physics in Medicine and Biology* **43** 887–94
- [31] Taguchi K, Zeng G L and Gullberg G T 2001 Cone-beam image reconstruction using spherical harmonics *Physics in Medicine and Biology* **46** 127–138